ELSEVIER

Contents lists available at ScienceDirect

Results in Surfaces and Interfaces

journal homepage: www.elsevier.com/locate/rsurfi



Self-assembly of exfoliated graphene flakes as anticorrosive coatings for additive manufactured steels



Kaleb Hood ^a, Wen Qian ^{b,*}, Yi Xia ^a, Savannah Krupa ^a, Annie Dao ^a, Sarah Ahmed ^a, Samuel Olson ^a, Nam Nguyen ^a, Joseph A. Turner ^b, Jun Jiao ^{a,*}

- Department of Mechanical and Materials Engineering, Portland State University, Portland, OR, USA
- ^b Department of Mechanical and Materials Engineering University of Nebraska-Lincoln, Lincoln, NE, USA

ARTICLE INFO

Keywords: Costing materials Thin films Crystal structure Corrosion Electrochemical reactions

ABSTRACT

This study demonstrates the feasibility of using liquid exfoliation of expandable graphite into multilayer exfoliated graphene flakes (EGFs) to form a self-assembled thin film on an air-water interface. The film can coat the surface of additive manufactured (AM) steel substrates to enhance surface properties, specifically AM 316 stainless-steel (AM316), AM 8620 steel (AM8620), and samples of the same alloys made by conventional manufacturing (CM) processes. Liquid exfoliation offers a high yield route for an EGF coating that can cover up to 95% of the sample surface with a single application. The thin, flexible EGFs can coat a rough AM metal surface, while the highly intact crystal lattice protects covered areas against diffusing ions and prevents localized corrosion compared to similar coatings made with graphene oxide (GO) or reduced GO (rGO). The EGF coating exploits a unique self-assembly process without surfactants or stabilizers, wherein the hydrophobicity and hydrophilicity of EGFs arrange the flakes, then van der Waals (vdW) forces bond them together and to the substrate for a coherent anti-corrosive coating. Electrochemical measurements indicate lower corrosion potential for coated samples, nanoindentation measurements show surface hardness protection against corrosive attack, and weight loss measurements demonstrate long-term protective capabilities. Density functional theory calculations, using the optB88-vdW exchange functional of the graphene and iron (111) interface demonstrated stronger binding and shorter interface distance compared to the well-studied graphene/nickel (111) interface. These calculations and experimental results can further elucidate the superior performance of EGF thin film coatings on high iron content steels, especially AM steels.

1. Introduction

Interest in graphene as a coating material has grown recently due to its chemical inertness, lubricating properties, thermal and electrical conductivity, hardening mechanisms, and anti-corrosive properties. Graphene exists in its natural form as thin sheets of hexagonal sp² bonded carbon atoms stacked and held loosely together with van der Waals (vdW) forces. Attempts to demonstrate graphene's anti-corrosive (Prasai et al., 2022) and surface enhancement (Kim et al., 2021) properties on metals show promise, but still face many challenges. Chemical vapor deposition (CVD) growth of graphene depends on the composition and microstructure of substrates, or requires a transfer process, limiting the choice of material and geometry (Xiaohui et al., 2015). Mechanical exfoliation and transfer from bulk graphite is a time intensive process limited in scale, geometry and is damaging to the exfoliated graphene (Kang et al., 2012). The graphene oxide (GO) synthesis process improves the yield of very thin sheets; however, the high temperatures and oxidizing chemicals not only result in sheets

that are highly defective, but are also in need of functionalization or combination with a polymer (Kumar et al., 2021). A standalone coating from GO can be made through the Langmuir-Blodgett method (Cote et al., 2009), which uses an air-deionized (DI) water interface and mechanical compression to coat substrates. The GO is then chemically or thermally treated to yield reduced graphene oxide (rGO). This process restores some properties of pristine graphene, but defects always remain. The reports by Jia et al. (2019) and Jia et al. (2017) demonstrated a modified Langmuir-Blodgett method in a double selfassembly process using rGO and surfactants to create coatings for 3D objects, but no mechanical or electrochemical measurements were presented. This study builds upon Jia's double self-assembly method, but uses liquid exfoliated graphene flakes (EGFs) to create coatings without the use of surfactants to assemble the film. By following the thermal expansion and liquid exfoliation technique developed early on by some authors in this study (Qian et al., 2009, 2013), a coating of low-defect and well-crystallized EGFs was created without the use of any surfactants.

E-mail addresses: wqian2@unl.edu (W. Qian), jiaoj@pdx.edu (J. Jiao).

https://doi.org/10.1016/j.rsurfi.2023.100116

Received 1 October 2022; Received in revised form 25 April 2023; Accepted 5 May 2023

Corresponding authors.

Metal additive manufacturing (AM) is an emerging technology with an array of possibilities for manufacturing (Tofail et al., 2018), where parts are built through a layer-by-layer local melting process or deposition of metal precursors. This process allows for part geometries and production procedures not available through conventional manufacturing (CM), including easy fabrication of metal alloys and composites, and reduction of material waste. Selective laser melting (SLM) is a type of metal AM that uses a laser to melt metal particle precursors to create a very dense final component with uniform elemental distribution. Ettefagh and Guo (2018) found that the higher density and uniform elemental spread in SLM results in a final product that already has higher corrosion resistance than CM processes, though the final products still suffer from a rough surface finish and porosity characteristic of AM products. These rough surfaces and anisotropic structures of AM metals likely act as corrosion sites (Schindelholz et al., 2021). While the AM product can be smoothed by chemopolishing or electropolishing (Tyagi et al., 2019), the 3D geometries which are an advantage of metal AM increase the difficulty of post processing, such as polishing rough surfaces. Creating an anticorrosive coating with high compatibility for an AM substrate, and the ability to coat 3D geometries will enhance the applications of AM metals.

The strengths of graphene-based coatings are chemical inertness, ion impermeability and conductivity (Chauhan et al., 2020). There are also challenges, which include the requirements of a high graphene yield for practical application to large areas, the ability to coat 3D samples, and good bonding to the target substrate. One common solution is dispersing GO/rGO in a polymer matrix (Chang et al., 2014) to create a tortuous path (Qi et al., 2015; Pourhashem et al., 2017; Nayak and Mohana, 2018), enhance polymer bonding (Parhizkar et al., 2017) to the substrate, or even coating rGO on a polymer surface (Su et al., 2014) to limit diffusion into the polymer. In all these cases, the GO/rGO is only an additive to improve a polymer coating that is already prone to damage, diffusion and delamination, all of which can accelerate the corrosion rate of the coated metal. Creating direct contact between high quality graphene and the metal substrate without a polymer improves the coating properties by directly blocking diffusing atoms to the surface and increasing the adhesion of the coating. CVD growth of graphene on CM steel was achieved by Dumée et al. (2015) who found that graphene acts as a conductive coating, decreasing the corrosion potential and localized corrosion of samples. However, coatings required growth times of 15 min for high coverage that resulted in coating thickness on the micron scale. Xu et al. (2019) used ball milling to exfoliate graphene from bulk graphite and simultaneously coat the surface of the ball with graphene. The electrochemical measurements suggest that the graphene coated surface had good anticorrosive properties, though the process seemed to be time intensive and damaging to the graphene. Moreover, this process is limited to spherical surfaces only. In the study reported here, the thermal-expansion and liquid-exfoliation of EGFs enables the pristine graphene lattice to be preserved, and the self-assembly process allows the graphene to be directly coated on the metal surface, without the requirement of surfactants or polymers in the EGF coating.

2. Materials, experimental and computational methods

2.1. EGF exfoliation

Fig. 1 shows the overall coating process. The expandable graphite precursor was purchased from ACS Materials (expansion temperature 180 °C and expansion volume 250 mL/g) and thermally expanded in a tube furnace to produce expanded graphite (EG) after a 30 min purge under argon flow. After the pure argon purge, hydrogen was introduced to create a forming gas (95% Ar and 5% $\rm H_2$) environment while the furnace was heated at a rate of 10 °C/min. After reaching 1000 °C, the furnace was maintained for 5 min, then quickly cooled to 200 °C and the EG removed. 10 mg from the top layer of EG in

the heating crucible was immediately added to 100 mL of N-Methyl-2-Pyrrolidone (NMP, Acros Organics >99.5% purity) and sonicated for 30 min with a 700-W probe sonicator (Qsonica). After sonication, the EGFs were centrifuged at 1000 rpm for 30 min, and the supernatant collected from the top 50% of the centrifuged solution. The resultant EGF/NMP solution was composed of multilayer graphene, with no unexfoliated graphite chunks, and was stable for several days without restacking. EGFs were resuspended in ethanol (EtOH) by centrifugation to remove NMP before creating a film. If not removed, the presence of NMP inhibited the quality of the final coating. The resuspension was carried out by centrifuging the EGF/NMP solution at 14,800 rpm for 5 min, pouring out and discarding the supernatant, adding 1 mL of pure EtOH, centrifuging again with the same parameters, then adding 300 μL of pure EtOH. This process can be performed repeatedly to further decrease the NMP concentration in the final product, however this will also decrease the EGF yield. After the above process, the concentration of EGFs was determined to be 1 mg/mL by evaporating the EtOH and weighing the remaining EGFs.

The "thermal-expansion liquid-exfoliation" process in this study yielded few-layer EGFs with graphene-like properties without any chemical modification to the EGFs, which can be assembled into a film on an air/DI water interface. The EGFs were stabilized in NMP until they were resuspended in ethanol (EtOH) for use (Johnson et al., 2015), and the thickness and lateral size of flakes can be selected by centrifugation speed (Khan et al., 2012). Films can be formed without surfactants by self-assembly through the amphipathic properties of EGFs and vdW bonding of sheets. The high crystallinity of the resulting film preserves the pristine graphene properties and contributes to the protective nature of the film, especially when applied to AM steel substrates.

2.2. EGF self-assembly and coating

The following description provides details on how an EGF film was formed and how the samples were coated by the EGF films; further discussion of the self-assembly mechanisms can be found in Section 3.1. Films were formed on DI water in a petri dish large enough to allow an excess of water compared to the EGF/EtOH solution while also having surface area sufficient for a film to coat the entire substrate. The EGF/EtOH solution was pipetted onto the water surface and the hydrophobicity of the EGFs enabled the flakes to quickly move to the air/water interface. EGF properties are consistent with those of multilayer graphene (Kuziel et al., 2020), in which the flake surfaces are hydrophobic, and the edges are hydrophilic. The flakes edges attract and overlap on the air/water interface and vdW bonding causes stacking. The film increased in density as more solution was added and eventually anchored itself to the petri dish or sample at the air/water interface. The film will not easily separate from the anchored area and can easily create a coherent coating from this spot. The sample can be dipped beneath and lifted through a film, or the solution drained to lower the film onto the substrate. Once coated, vdW forces adhere the coating to the surface of the sample, then samples were left to dry ambiently. The largest steel samples used in this study were 1 cm³ based on the size limits of the testing equipment, although a larger coating area simply requires a larger container and more EGF/EtOH solution, because the EGFs will spread to cover the surface of the DI water. Films up to three inches in diameter have been formed to coat CM316 samples up to two inches in size. To measure the structural and chemical properties of EGFs, Raman spectroscopy (Horiba Jobin Yvon HR800 with 532 nm laser) was performed on an EGF coated silicon wafer. To determine the effect of a corrosive solution on the EGF coating, a coated silicon wafer sample was submerged in 5 wt% NaCl/DI water solution for 14 days. Three 20 μ m \times 20 μ m square areas (accumulatively, 400 spectra per area were obtained) were mapped, with the mean 2D:G and D:G ratios calculated. The same sample areas were mapped again after exposure to the NaCl solution to compare the ratios. After the coating process was refined and the EGF films characterized on silicon wafers, the coating technique was applied to AM samples.

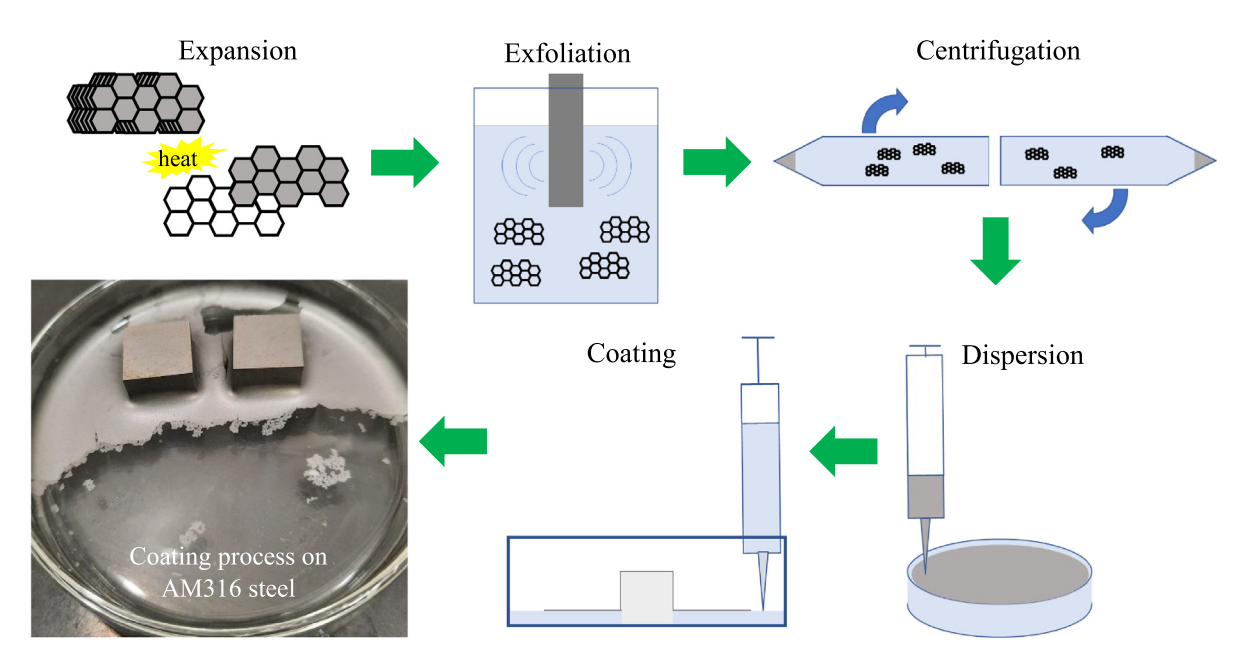


Fig. 1. Experimental procedure, following the green arrows, for EGF coatings: thermal expansion of EG precursor; liquid exfoliation to form EGFs through sonication in NMP; centrifugation and resuspension; dispersion across the DI water surface to create a film; lowering the water surface to coat an AM cube; image of coating being applied to two AM316 cubes. (For interpretation of the references to color in this figure legend, the reader is referred to the web version of this article.)

Table 1The specific elemental composition of 316 and 8620 steel alloys in AM samples. These compositional contents are consistent with their CM counterparts (the unit of the contents in the Table is wt%).

	Fe%	Cr%	Ni%	C%	Mn%	Mo%	P%	Si%	S%	N%
316 steel	62-69	16–18	10–14	0.08	2	2-3	0.045	0.75	0.03	0.1
8620 steel	97–98	0.4-0.6	0.4-0.7	0.18 - 0.23	0.7-0.9	0.15 - 0.25	0.035	0.15 - 0.35	0.04	NA

2.3. Additive manufactured steel samples

The metals selected for this study were additive manufactured 316 stainless steel (AM316) and additive manufactured 8620 (AM8620) mild steel, with CM samples (CM316) and (CM8620) used as controls in some corrosion tests. The elemental compositions are consistent between CM and AM steel samples as shown in Table 1. Both 316 and 8620 steels were selected for this study because of their high iron content to demonstrate the capabilities of the EGF coatings for corrosion protection of iron-rich alloys. The AM samples were printed as cubes (10 mm side length) using a laser powder bed fusion (LPBF) system, a type of SLM, equipped with a three-axis machining center (Matsuura Lumex Avance-25). During the manufacturing process, the build plate temperature was set to 50 °C, and the working chamber was filled with nitrogen gas (consisting of no more than 3% oxygen) to prevent oxidization of the molten pool during laser melting. A bidirectional laser scanning strategy with a 90° rotation after every layer was used for LPBF printing at 4 different powers - 160, 240, 320, and 380 W - which were used for both the rastering/infill and contouring passes. The laser scan speed was 700 mm/s, the spot diameter was 0.2 mm, the hatch distance was 0.127 mm, and each layer's thickness was 0.05 mm.

2.4. Nanoindentation

The localized mechanical properties (modulus and hardness) of the AM metal samples were measured using a Hysitron TI 950 Triboindenter through quasi-static nanoindentation. A Berkovich (three-sided pyramid) diamond tip was mounted on a transducer that allowed for displacements in the z-direction. During an indentation measurement, the tip was pressed into the sample such that the resulting forcedisplacement behavior was quantified. A total of nine (3 \times 3 array) indents in three different regions were made on each sample with $20~\mu m$ of spacing between indents. The indentations were made with a target force of 10~mN at a constant loading rate of $400~\mu N/s$. The indentation procedure included a linear loading ramp of 15~s,~a holding period of 10~s at the maximum load and a linear unloading ramp of 15~s. The load–displacement unloading curves from each indentation were used to fit and calculate the hardness (H) for the sample using the Oliver–Pharr method (Oliver and Pharr, 1992; Pharr et al., 1992).

2.5. Electrochemical testing

Electrochemical tests for all samples were performed with a Gamry Reference 600 Potentiostat/Galvanostat with a three-electrode set-up using a graphite counter electrode and saturated calomel (SCE) reference electrode in a 3.5 wt% NaCl/DI water solution. A 3.5 wt% solution for electrochemistry was selected to match the common electrolyte concentration used in other studies (Ettefagh and Guo, 2018; Dumée et al., 2015; Xu et al., 2019) on graphene coatings on metal instead of the 5 wt% NaCl/DI water used for the corrosive solution in weight loss and nanoindentation tests. Corrosion current (I_{corr}) and corrosion potential (E_{corr}) were calculated using the Gamry Framework and Echem Analyst software of the potentiostat. Electrode samples were embedded in epoxy resin (Ted Pella Inc) to isolate the working electrode surface (surface area $\approx 1.5 \,$ mm²). Before electrochemical testing, all samples were polished, then samples for coated measurements received a single coating of the EGF film.

2.6. First-principles simulations

The first-principles simulations based on density functional theory (DFT) were performed to understand the binding mechanism of the graphene/steel interface, aimed at establishing the correlation between

the EGF coating films and the metal surfaces. Steels are primarily composed of iron with other minor alloving elements, so a simplified interface model was used for the computation in this study. The model is composed of monolayer graphene, a fcc-iron (111) surface made of six layers of metal atoms, and a vacuum region of more than 10 Å. To reveal the relative strength of binding, a comparative study of the graphene/fcc-iron(111) interface against the graphene/fcc-nickel(111) interface was performed. The latter has been well investigated and recognized to have a strong interfacial binding (Dedkov and Fonin, 2010). The specific symmetrical configurations of graphene on both Ni(111) and Fe(111) surface were chosen based on Zhang et al. (2014), where the top-fcc has been found to exhibit the lowest energy. The experimental lattice parameters for fcc-Ni (=3.53 Å) and fcc-Fe (=3.57 Å) were used. Since both lattice parameters show a relatively small mismatch with the lattice parameter of graphene, 1.5% mismatch for Ni and graphene and 2.6% for Fe and graphene, this allowed the in-plane lattice parameter of the interface structure to be fixed while allowing the out-of-plane relaxation of atomic positions. After relaxation, the interfacial binding profile was mapped out by rigidly displacing the graphene at varying distances away from the metal surface.

3. Results and discussion

3.1. EGF self-assembly, film structure and chemical properties

The EG is a polycrystalline graphite intercalation compound, for which thermal expansion separates the graphene layers and weakens the interlayer vdW attraction. This increases the yield of few-layer graphene in the liquid exfoliation process with less damage to the crystal lattice. The advantage of this exfoliation method over the Hummers method (Hummers and Offeman, 2022) for GO is that exfoliation of EG happens readily without chemical modification to the sp² bonding through the bulk of the flake, maintaining the high crystallinity. The physical properties, which drive the self-assembly for EGFs, are based on the thickness of exfoliated flakes and the lateral dimensions. Monolayer graphene has hydrophilic edges and surfaces (Belyaeva et al., 2018). Multilayer graphene maintains edge hydrophilicity while becoming more hydrophobic with increasing number of layers (Munz et al., 2015). Since EGFs are multilayer, the edges will be hydrophilic and planar surfaces will be hydrophobic. These properties cause the movement of EGFs to the water surface when the EGF/EtOH solution is added to the petri dish. As EGFs spread across the air/water interface, the hydrophilic edges collect a thin layer of water (Kuziel et al., 2020) and the wetted edges will attract other EGFs. The combination of the dispersive hydrophobic forces and attractive hydrophilic forces cause the EGFs to pack tightly and the edges to overlap. Adding more solution causes EGFs to overlap more, increasing the density and coverage. Since graphene suspensions restack (Johnson et al., 2015) through vdW bonding of surfaces, in the absence of a stabilizer, the overlapping EGF edges can bond through vdW attraction of surfaces. Once bonded, they will resist separation, resulting in a rigid and integrated film. It is important to control and optimize the density of the EGFs to control the thickness and coverage of the EGF thin film. A fully integrated film can survive light shaking of the petri dish and will even attach to another film whether bonded to a substrate or floating in the dish. When the film is lowered onto a silicon wafer or steel surface, vdW forces act to bond the coating to the substrate, and as the solution evaporates from the drying sample, the bonding will increase in strength from the interaction between the bulk EGF surface and the substrate. Removing NMP from the EGF surfaces by resuspension is critical for the final film quality, because NMP is a stabilizer that will interfere with vdW attraction between the graphene and substrate surface, as well as the graphene sheets bonding to each other. A comparative experiment was carried out by adding surfactants to the solution in the petri dish, following the methods by Jia et al. (2019). The results suggested that the surfactants interrupted the EGF self-assembly process, and the

resulting film was less dense. Small EGFs have properties similar to monolayer graphene, where the hydrophilicity of edges and surfaces drives them to aggregate in a disordered manner on the larger flake edges and to each other. This results in a coating of few-layer EGFs in spaces between larger flakes and even in the areas of larger gaps. These edge properties of EGFs can further be explained by work with GO which focuses on properties of dangling bonds and functional groups for flakes/film properties (He et al., 2017; Shih et al., 2022). These dangling bonds influence the hydrophilic properties of the flake and make it easy to coat a hydrophilic surface like steel. The strength of inter-flake bonding for dense EGF films allowed the film to hold together, even when coating substrates at challenging angles, such as the vertical edge of a cube or hydrophobic surfaces, like an untreated silicon wafer. Tuning the EGF film formation to better coat difficult geometries and to optimize coatings are areas of interest for future research.

Fig. 2 shows SEM images (SNE 4500-M Plus) of EGF films deposited on a silicon substrate. As indicated in Section 2.2, a silicon substrate was used to improve the ease of testing EGF coatings and for more accurate Raman characterization because the AM metal surface may obscure the EGF Raman peaks. Furthermore, the flat silicon wafer surface was beneficial for measuring the thickness of EGF films. Fig. 2(a) shows a large, coated area with coverage of 85%-95% over a 300 µm \times 250 µm area. The high coverage comes from EGFs that were lying flat on the substrate or are overlapping each other to create a flat film. In some areas EGFs can be seen stacked at an angle. Fig. 2(b) is a higher magnification image where EGFs can be seen arranged edge to edge with a thin gap between the flakes, or in overlapping stacks. Areas not covered by large EGFs are typically 4 µm or smaller, also shown in (b). High resolution SEM images and Raman spectroscopy confirm that these areas are coated with the very thin EGFs. These thin EGFs can either be large sheets as shown in Fig. 2(c), or they can be small diameter fragments that collect at larger flake edges and inside gaps. Most large EGFs are 1-8 µm in size, and smaller ones have been detected about 100 nm in size. The wrinkles on the flake surfaces and flexibility of stacked layers shown in Fig. 2(c) are consistent with other reports of the flexibility of multilayer graphene (Stöberl et al., 2022). This flexibility is what allows multiple EGF coatings to easily overlap with previous coatings and conform to the rough surface of AM metals to create a diffusion barrier, which achieves the anticorrosive coating purpose.

The linescan profile in Fig. 2(d) is along a path from a gap coated with thin EGFs, across an area of coating film, then to an uncoated gap. The line profile at 0 μm, as marked in Fig. 2(d), is 20 nm in height, which correlates to ~20–30 layers, and the minima along the scan range are from 5-20 nm for 10-30 layers. The overlapping regions are 60-80 nm in height, with a few angled EGFs over 100 nm. A second coating increases the thickness to around 150 nm. The laser height profile map in Fig. 2(e) shows a 45 μm scanned square with most of the film under 100 nm. The high areas are typically 1.5 μm up to 3 μm , as marked in yellow and red respectively in the color bar in Fig. 2(e). These results are consistent with the size of the EGFs angled out from the EGF coating on the sample. Most gaps in the EGF coating are actually covered by very thin EGFs, as seen by the dark blue coloration. The edges of the larger EGFs are sloped due to the smaller EGFs aggregating against them. Raman spectroscopy suggests that the 60-80 nm height of films is due to the overlapping of thinner flakes.

Fig. 2(f) shows examples of Raman spectra for flakes in the sample. The main peaks interpreted are the G and 2D peaks, which can be used to determine the thickness of graphene, and the D peak which is a measure of disorder, defects and edges. In this study, the Raman spectroscopy is used to characterize graphene's crystalline properties through the ratio of the D and G peaks, where a low ratio corresponds to high crystallinity and low defects. The thickness was approximated through the shape of the 2D peak, position of the G peak and the ratio of 2D and G peaks (Ferrari and Basko, 2013). In Fig. 2(f), the spectrum in

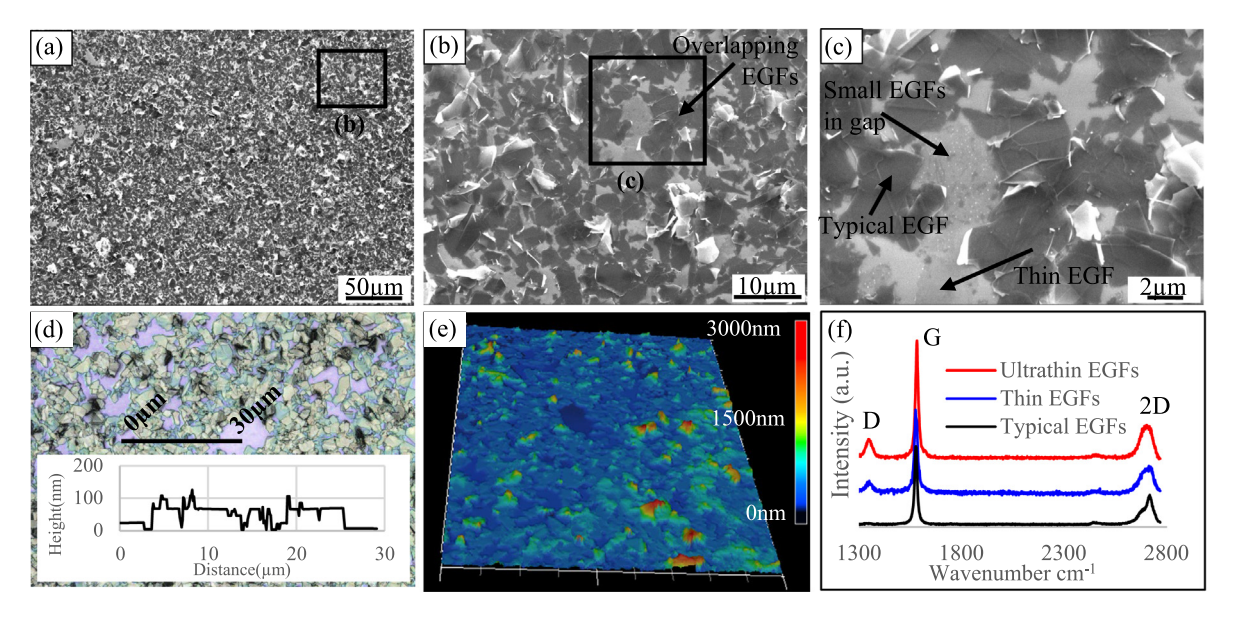


Fig. 2. (a) SEM image of EGF coating on a silicon wafer showing uniformity of coating over a large area; (b) Detail from (a) showing the coating in a gap, and the relative size of most EGFs between 1 μ m and 8 μ m; (c) Detail of flake morphology from (b) with small EGFs shown in the gap and a large thin exfoliated sheet. Wrinkles can be seen on the surface of some EGFs, characteristic of exfoliation; (d) laser scanning microscope image with 30 μ m laser height profile linescan showing the majority of the film less than 100 nm thick; (e) 3D height map from the same image showing relatively flat film; an area in the center is uncoated and almost all other low areas are filled with a ultrathin film of EGFs; (f) Raman spectra where the black spectrum is obtained from typical EGFs; the blue spectrum was taken from the thin EGFs; and the red spectrum was taken from the ultrathin EGFs in gaps. (For interpretation of the references to color in this figure legend, the reader is referred to the web version of this article.)

black is the most common for EGFs, representing 10+ layer graphene. The minimal D peak is evidence that the sp² bonds present in the EG precursor are not damaged in most of the film. The Raman spectrum changes dramatically as graphene layers decrease below 10, with the spectra in blue and red showing thin EGFs (6-10 layers) and ultrathin EGFs (2-5 layers) in the gaps respectively. The 2D peak shifts to lower wavenumbers while the G peak increases in wavenumber, and the 2D peak also changes in shape (Ferrari and Basko, 2013). A plausible explanation for the appearance of the D peak in both blue and red spectra could be attributed to the reduced lateral size of EGFs during the creation of thin EGFs. To create thin EGFs, the sonication processing must be aggressive, leading to smaller EGF pieces. The smallest pieces have a lateral size of 100 nm, while the Raman laser spot size is around 1 μm. When the laser spot size is larger than the size of the EGFs, the edges of the EGFs manifest as defects in the Raman spectra, and more small pieces under the Raman laser spot will increase the D peak. Note that the spectra in blue and red are marked as thin and ultrathin respectively.

The quality of the EGFs was further examined with Raman mapping as shown in Fig. 3 where (a) is the optical reference image for Raman mapping. Fig. 3(b) shows the high crystallinity of the film by using the D:G ratio. The low defect ratio (<0.01) is represented in green and covers most of the film. Flake edges and coated gaps are shown in yellow, due to the increased D peak from edge effects and ultrathin EGFs. The 2D:G peak ratio was used in Fig. 3(c) to determine the thickness of the EGF film. Thick regions are represented in blue and thin regions in green, with the average ratio being 0.26 (between 0.15 and 0.4) in this sample. Black spots are from Raman spectra without a significant peak in comparison to the background or lost in substrate fluorescence. The inserted mini-Tables in (b) and (c) suggest that the 2D:G and D:G ratios did not significantly change when a different sample was submerged in a 5 wt% NaCl/DI water solution for 14 days (with characterization performed on day 7 and 14). These results suggest that the EGF coating films exhibit good crystallinity and resistance against NaCl corrosion.

3.2. Mechanical properties of EGF coated surfaces

Based on the promising qualities of the EGF films characterized by the techniques described above, the steel samples (AM316 and AM8620) were coated with EGF films, then the investigation of the hardness of AM316 and AM8620 was carried out. The coated and uncoated samples were submerged in a 5 wt% NaCl/DI water solution for 10 days. The hardness testing results are shown in Fig. 4. The hardness of a metal in nanoindentation is based on the elemental composition of the bulk metal and the passive layer formed on a metal surface. Thus, by comparing the elements present in AM316 and AM8620, insights can be gained by nanoindentation characterization. When exposed to a corrosive solution, elements like iron that corrode more easily leach from the sample in the form of ions, leaving the other elements behind and reducing the surface hardness. In Fig. 4, the lower initial hardness of AM316 compared to the AM8620 is affected by chromium and nickel alloying elements, as well as other elements shown in Table 1. Due to the passive chromium oxide layer that quickly formed on the stainless-steel surface of AM316 during corrosion, the underlying surface has little change in hardness as demonstrated in Fig. 4(a) whether coated or uncoated after 10 days of corrosive testing. Though the hardness change was small for AM316, it should be noted that material was still lost from the surface through corrosion, as shown in the electrochemical and weight loss testing data in Section 3.3. The higher corrosion rate for the iron-rich AM8620 (97-98% iron in AM8620 compared to 62-69% iron for AM316), and the protection of the surface hardness by the EGF coating is more visible in Fig. 4(b). After 10 days in the corrosive solution, the hardness of the uncoated sample is reduced to half (~50%), from 13.59 GPa to 6.87 GPa. When protected by the EGF coating, the underlying metal surface has a 6.5% lower reduction in hardness compared to the uncoated metal. This suggests that the EGF coating protects the surface by minimizing the leaching of iron. This is due to the EGFs ability to limit the ion diffusion of corrosive salts and metal corrosion products. While the EGF coating films need to be further optimized, the results obtained by corrosion testing and nanoindentation testing are very promising.

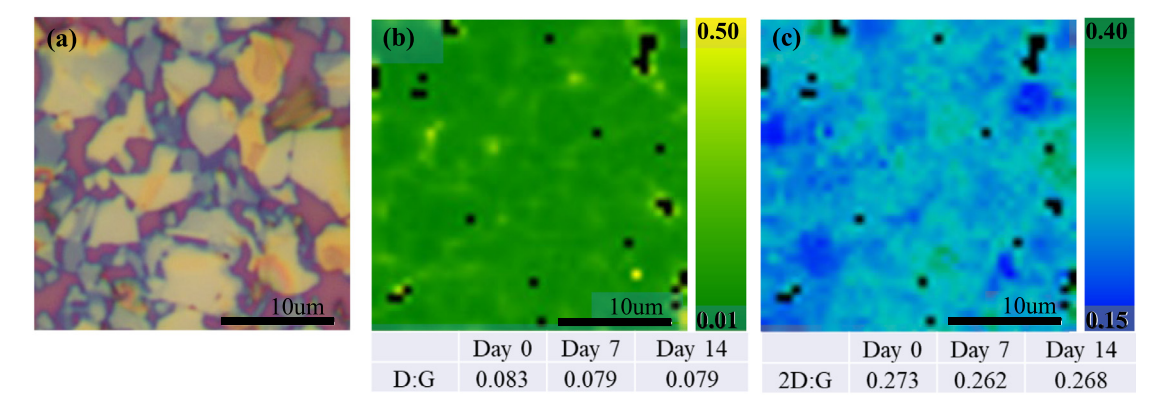


Fig. 3. Raman ratio maps of a 20 μ m by 20 μ m coating area showing quality of EGFs and coverage. (a) EGF coating with purple areas appearing as exposed silicon wafer, which are coated by ultrathin EGFs; (b) Map for D:G peak where the centers of flakes show the low ratio of \sim 0.01 for minimal defects, and the higher ratio in yellow matches flake edges as well as the coating in gaps; (c) Ratio map of graphene 2D:G ratio with the average ratio of \sim 0.26 for the film. Thick regions of the film are represented with blue, and thin areas are shown in green, with the ultrathin EGFs clustered on edges and in gaps; The inserted mini-tables in (b) and (c) are for an EGF coated silicon wafer that was submerged in 5 wt% NaCl/DI water solution for 7 then 14 days. (For interpretation of the references to color in this figure legend, the reader is referred to the web version of this article.)

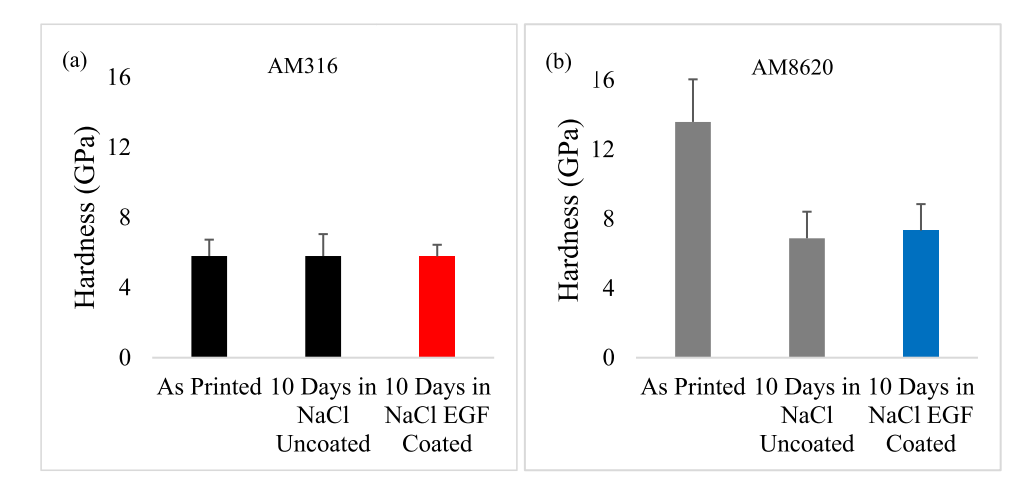


Fig. 4. Hardness measured by nanoindentation for AM316 and AM8620 samples before and after soaking in 5 wt% NaCl/DI water solution compared to surface protection for coated samples. (a) As-printed AM316 after 10 days in NaCl solution uncoated and coated showing the significant anticorrosive capability of the EGF coating films.

3.3. Electrochemical properties of EGF coated samples and weight loss measurements

Testing the corrosion of steel by weight loss in a NaCl/DI water solution can reinforce the results uncovered by nanoindentation because as iron leaches from the surface in the form of ions, a simultaneous loss of mass and surface hardness occurs. Measuring corrosion of steel by weight loss over time also shows a coating's long term protection of a surface. Fig. 5 shows the weight loss measurements for uncoated and coated steel samples in a 5 wt% NaCl/DI water solution for 28 days. For both steels, the results indicate the CM sample weight loss rate was higher than AM samples. One plausible reason for this is the higher density of the AM steel (Ettefagh and Guo, 2018). For the 316 steel samples, shown in Fig. 5(a) the coated CM316 (brown and purple) samples showed a decreased weight loss rate over 28 days, from 0.033 mg to 0.028 mg (~15%). The already lower rate for AM316 (black and red) decreased from 0.020 mg to 0.013 mg (~35%) when coated. Because 8620 steel is mostly iron, the CM and AM 8620 steel samples lose weight at a rate an order of magnitude higher than AM and CM 316 steel. However, the improvement to weight loss by coating samples was significantly larger for the 8620 steel, as shown in Fig. 5(b). The CM8620 (light gray and green) rate decreased from 0.59 mg to 0.22 mg (~61%), and the AM8620 (dark gray and blue) decreased from 0.34 mg to 0.18 mg (~47%). These results demonstrate that the EGF coated 8620 steel will corrode at half (\sim 50%) the rate of an uncoated sample. The EGF coating offers significant protection against corrosive solutions for high iron content steel, by preventing ion loss from the metal surfaces. After 28 days the EGF films still showed protection of the surface.

Electrochemical testing was used to gain further insight into the protective capabilities of EGF coatings through potentiodynamic polarization. A total of 20-25 samples were tested for each AM steel. This procedure was used to establish an experimental baseline for the elemental composition and SLM printing parameters used in this study for comparison with others. While CM316 is a heavily studied material for its electrochemistry, the reported data concerning the electrochemical properties of AM316 and graphene coatings on high iron content steels such as CM8620 and AM8620 are very limited. Ettefagh and Guo (2018) found that CM316 had a corrosion potential of -471 mV, while the AM316 was lower at -362 mV due to the higher density of AM parts. The average corrosion potential of the AM316 used in this study was -296 mV, shown as a potentiodynamic polarization curve in Fig. 6(a) in black. Although the measured value is 66 mV lower than the data reported by Hemmasian et al. the lower value of the AM316 is largely due to the specific processing parameters and the counter electrode material used in this study. The baseline corrosion potential for AM8620 was also determined experimentally. To our knowledge, this is the first report of the electrochemical properties of as-printed

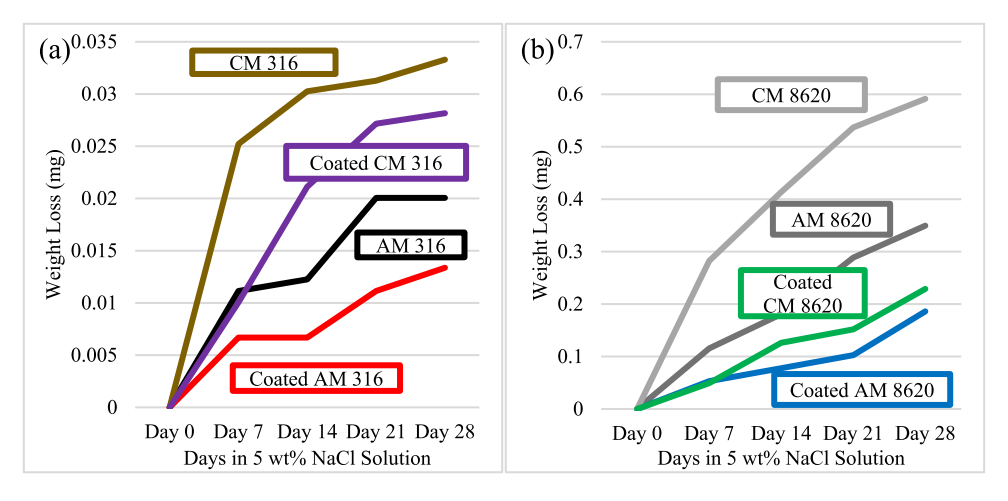


Fig. 5. Weight loss measurements of CM and AM samples, coated and uncoated. (a) Weight loss of 316 steel cubes after 28 days in a 5 wt% NaCl/DI water solution; (b) The same as (a) but for 8620 steel cubes. (For interpretation of the references to color in this figure legend, the reader is referred to the web version of this article.)

AM8620 samples as well as AM8620 samples with EGF coatings. The corrosion potential of the uncoated AM8620 at -537 mV is shown as a potentiodynamic polarization curve in Fig. 6 in gray. The higher rate of weight loss for this sample compared to AM316 is reflected in the higher corrosion potential, because AM8620 has a much higher iron content. After coating the samples with EGFs, AM316 showed a positive shift from -296 mV to -265 mV and AM8620 showed a positive shift from -573 mV to -559 mV shown by the plots in red and blue respectively (Fig. 6(a)). This positive shift shows that the EGF coating makes the surface more cathodic and resistant to corrosion. Graphene coating methods involving CVD growth of graphene on steel surfaces (Xiaohui et al., 2015; Dumée et al., 2015) or mechanical transfer of graphene on spherical samples by ball milling (Xu et al., 2019) resulted in a large positive shift in the corrosion potential due to the complete coverage of the graphene. The smaller positive shift in the corrosion potential of the EGF coated samples suggests that by improving the coating for complete coverage the positive shift in the potential will increase further.

One challenge for metals exposed to a corrosive solution is how the variation in the microstructure or surface finish leads to the formation of cathodic and anodic sites on the metal surface. The anodic sites have an increased rate of corrosion, which can lead to pitting or crevice corrosion, and eventually to cracking and material failure. This phenomenon is especially true for AM steels, because even though the dense components have a lower corrosion potential, the surface porosity, roughness and residual stresses in the melt pool boundaries from the laser can act as sites for pitting corrosion (Schindelholz et al., 2021). One concern about graphene coatings is that the inert graphene will act as a cathode to the metal, which was seen when a GO coating was applied to mild steel through electrophoretic deposition (Park and Park, 2014), or through functionalization (Ansari et al., 2020). However, in the study by Dumée et al. (2015) a CVD grown graphene coating with high coverage and good crystallization prevents the formation of cathodic/anodic sites. The increase in corrosion current and narrowing of the polarization plots are attributed to the conductive graphene coating increasing surface conductivity and the isolation of the metal surface from the electrolyte to prevent ion diffusion. In this study, the polarization curves for the AM316 showed a small increase in the corrosion current from an increase in surface conductivity, but minimal change to the shape of the plot. Thus, even though the corrosion potential of AM316 was reduced by the EGF coating, any uncoated areas were protected by chromium oxide passivation, which isolated the iron from the corrosive solution. In contrast, the AM8620 showed a larger increase in current and plot narrowing, because the diffusionblocking properties of the EGF coating have a greater protection effect on the high-iron alloy. It was observed that uncoated AM8620 samples

after electrochemical tests would develop deep pits in the metal surface with large amounts of corrosion products being deposited around the pits, as shown in Fig. 6(b). The coated samples shown in Fig. 6(c) have no pits and any corrosion products typically initiated from the sample edge. These results, especially for the AM8620, demonstrate that the well-crystalized EGF coatings directly bonded to the metal surface isolate the coated surface from diffusing ions in the corrosive solution and delocalize the corrosion to prevent pitting. By combining EGF coatings and AM processes, steel samples can be made with a lower corrosion rate than CM processes, and a resistance to localized/pitting corrosion.

3.4. Interfacial binding properties of Iron and graphene

Since the effectiveness of graphene coatings on metals and steels for promoting anticorrosive properties relies highly on the interaction between graphene and the surface of the substrates, the key to further improving the anticorrosive performance lies in a comprehensive understanding of the interfacial binding properties of graphene/metal interfaces. The literature has reported a strong interfacial binding between graphene/Ni, graphene/Co, or graphene/Ru surfaces, and weak interaction between graphene/Cu, graphene/Au, or graphene/Pt surfaces (Adamska et al., 2012). Considering the limited reports on theoretical calculations for the interaction between graphene/Fe surfaces, it is of fundamental importance to reveal their binding behavior and to understand the mechanism underlying the obtained experimental results.

Fig. 7(a) and (b) shows the simulation model, composed of monolayer graphene, an fcc-iron (111) surface made of six layers of metal atoms, and a vacuum region of more than 10 Å. The top-fcc symmetrical configuration of graphene on both Ni(111) and Fe(111) surface is shown in Fig. 7(c), based on Zhang et al. (2014) because it exhibits the lowest energy. Fig. 7(d) shows the plots for the calculated interfacial binding energies per graphene (two carbon atoms) as a function of distance for the graphene/Ni(111) interface (blue line) and the graphene/Fe(111) interface (red line), respectively. Interestingly, the two interface structures exhibit a somewhat different binding energy profiles; the graphene/Ni(111) interface displays two separated and shallow energy minima, while the graphene/Fe(111) interface exhibits a single and deep energy minimum. The calculated binding energy profile with double energy minima for the graphene/Ni(111) interface agrees well with Zhang et al. (2014) in both magnitude and shape when the same exchange-correlation functional, i.e., optB88-vdW was employed for both studies. Specifically, the calculated binding energy of graphene/Ni(111), in this study, shows a value of about -0.15 eV/graphene while Zhang et al. calculated value is -0.14 eV/graphene,

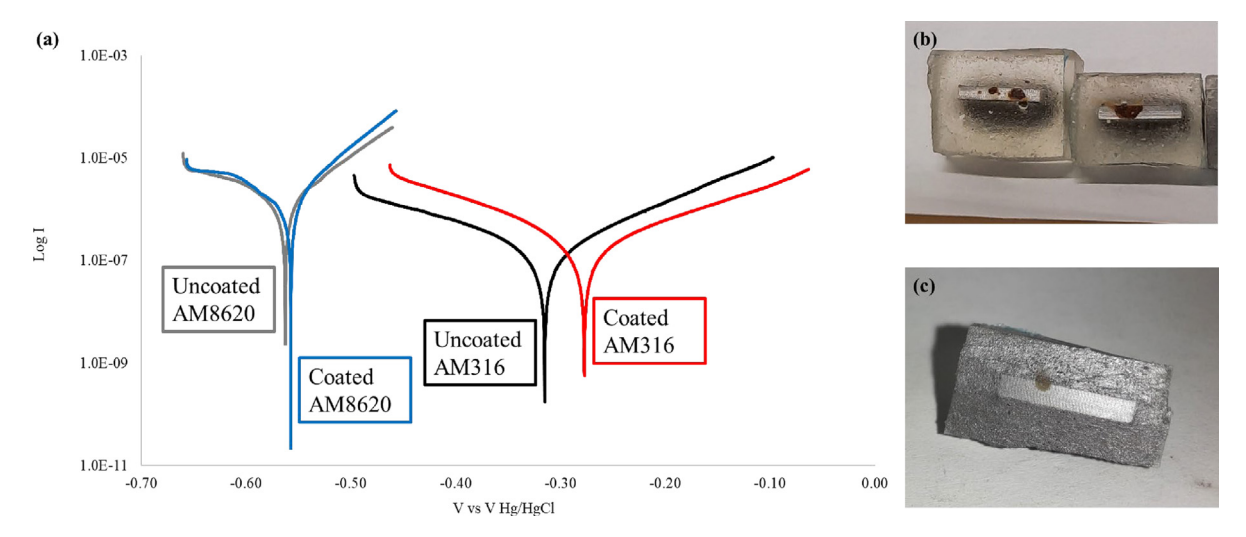


Fig. 6. Electrochemical tests for AM8620 and AM316 samples using a 3.5 wt.% NaCl/DI water electrolyte before and after coating. (a) The potentiodynamic polarization tests for AM8620 samples with a sweep range of \pm 100 mV vs. the open circuit potential (E_{oc}) and AM316 with a sweep range of \pm 200 mV vs. E_{oc} . (Note: Representative curves were selected from experimental data to show the EGF protection capabilities) (b) An uncoated AM8620 electrode sample after testing and (c) a coated AM8620 electrode after testing. (For interpretation of the references to color in this figure legend, the reader is referred to the web version of this article.)

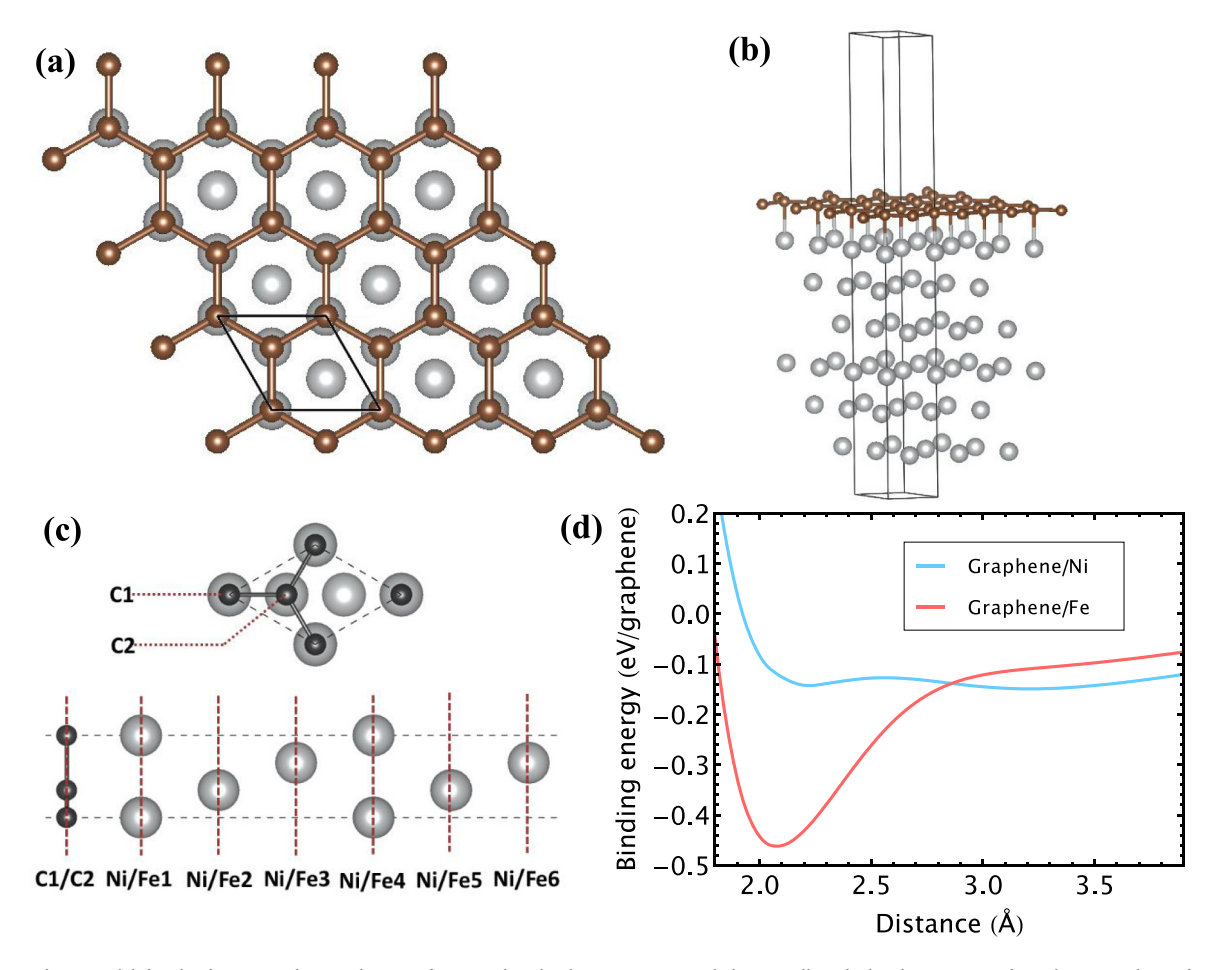


Fig. 7. Iron-graphene model for the first-principles simulations of iron-carbon binding properties and theoretically calculated properties of graphene/metal interfaces. (a) Top view of lattice match for graphene and fcc metal (111) surface; (b) Side view of space filling model of graphene on the fcc metal (111) surface, with lines indicating the unit cell used for simulation; (c) Geometries of the top-fcc interface structure composed of graphene and metal (111) surface. The black spheres represent the carbon atoms, while the gray spheres represent the metal atoms (Ni and Fe). The carbon atoms have two symmetrically inequivalent states, denoted as C1 and C2, respectively. The metal atoms (Ni and Fe) are indexed from one to six according to their distance away from the graphene. Section taken from area indicated in (a); (d) Binding energies of graphene on Fe/Ni(111) surface as a function of distances between graphene and metal surfaces. (For interpretation of the references to color in this figure legend, the reader is referred to the web version of this article.)

further validating the effectiveness of the calculation methodology and the parameters used in this study. Using the same computational parameters, the calculated binding energy for the graphene/Fe(111) interface was -0.44 eV/graphene, characterized by a much steeper potential energy surface. This finding indicates that the substrate adhesion is much stronger for Fe than Ni, suggesting that the application of graphene flakes as coating materials on steels is superior to other transition metals.

Although the above results demonstrate the superior interfacial binding properties of the graphene/Fe(111) interface as compared to the graphene/Ni(111) interface, these calculations are approximated at the level of density functional theory with a specific form of the exchange correlation functional, namely, optB88-vdW (Dedkov and Fonin, 2010). The literature has reported that the computed interfacial binding energy and the optimal interface geometry highly depend on the adopted exchange-correlation functional and vdW interaction model. For instance, the local density approximation (LDA) functionals seem to correctly predict the strong and weak binding between graphene and metals (Adamska et al., 2012), while the generalized gradient approximation (GGA) functionals yield no binding (Adamska et al., 2012). Meanwhile, despite vdW functionals describing the nonlocal dispersive interactions more accurately, the absolute values of binding energy calculated using different vdW functionals vary significantly (Dedkov and Fonin, 2010). Therefore, it is proposed that the trend in interfacial binding properties uncovered by this study is more reliable than the absolute values (e.g., binding energies). Indeed, the larger binding energy of the graphene/Fe(111) interface indicates a stronger binding between the Fe(111) surface and the graphene. The corresponding deeper potential energy surface suggests that the most stable interface geometry is more attainable in the graphene/Fe(111) interface, which might be further improved by proper annealing to the lowest-energy configuration. Furthermore, these results imply the potential feasibility of attaining a reliable coating of graphene flakes on steels to enhance the surface properties.

4. Conclusion

The self-assembly method for EGF coatings reported in this study shows a promising and less complicated method to create an anticorrosive thin film graphene coating. Characterization through Raman spectroscopy suggests that the graphene obtained by the "thermalexpansion liquid-exfoliation" is of high crystal quality with minimal defects. The synergistic effects of hydrophilicity and hydrophobicity of EGFs, along with vdW attractive forces, allow the EGF film to form on the surface of DI water through a unique self-assembly process. The coating method shows potential for applying a graphene coating to the 3D geometry of CM and AM steels, especially those with a high iron content. Furthermore, the "thermal-expansion liquid-exfoliation" process used in this study enables selection of EGFs with different sizes. This allows large flakes to contribute to high coverage and smaller EGFs cover gaps. The surfactant-free and polymer-free coating film has the advantage of EGFs bonding directly with the metal substrate. The strong binding between carbon atoms in graphene and iron atoms in steel, revealed by the theoretical calculations, not only aid understanding of the atoms' binding behaviors, but give an in-depth understanding of the underlying mechanisms for the obtained experimental results. These experimental results suggest that as a corrosion barrier, EGF coatings are effective due to their ability to delocalize corrosion and isolate the metal substrate from a corrosive solution. Electrochemical measurements reveal that EGF coatings decrease the AM steel's potential to corrode and prevent localized corrosion. The preserved hardness of AM8620 surfaces by EGF coatings and the decreased weight loss rates for all coated samples are all evidence that the EGF coatings successfully isolated the metal surfaces from the corrosive solution to prevent leaching of iron from the steel. To improve the quality and effectiveness of the EGF coating films, further efforts are needed

with emphasis on systematic optimization of the EGF flake size and thickness. This work will be combined with theoretical validation of the experimental results, and methods to improve the coverage and adhesion to the substrate.

Declaration of competing interest

The authors declare that they have no known competing financial interests or personal relationships that could have appeared to influence the work reported in this paper.

Data availability

Data will be made available on request.

Acknowledgments

This research is funded in part by the Oregon Metal Initiative, Intel Corporation, and the National Science Foundation (Award No 1711994). The participation of undergraduate students to this research is supported by National Science Foundation REU-Site (Award No. 1851851). Experiments and characterization were performed at the Portland State University Nanodevice Fabrication and Nanomaterial Synthesis Labs, and the 3D printed steel manufacturing and nanoindentation tests were performed at the Nebraska Engineering Additive Technology (NEAT) Labs, Nano-engineering Research Core Facility (NERCF) of the University of Nebraska-Lincoln, which is partially funded by the Nebraska Research Initiative.

References

- Adamska, L., Lin, Y., Ross, A.J., Batzill, M., Oleynik, I.I., 2012. Atomic and electronic structure of simple metal/graphene and complex metal/graphene/metal interfaces. Phys. Rev. B 85 (19), 195443. http://dx.doi.org/10.1103/PhysRevB.85.195443.
- Ansari, K.R., Chauhan, D.S., Quraishi, M., Saleh, T.A., 2020. Bis(2-aminoethyl) amine-modified graphene oxide nanoemulsion for carbon steel protection in 15% HCl: Effect of temperature and synergism with iodide ions. J. Colloid Interface Sci. 564 (March), 124–133. http://dx.doi.org/10.1016/j.jcis.2019.12.125.
- Belyaeva, L.A., van Deursen, P.M.G., Barbetsea, K.I., Schneider, G.F., 2018. Graphene: Hydrophilicity of graphene in water through transparency to polar and dispersive interactions (Adv. Mater. 6/2018). Adv. Mater. 30 (6), 1870041. http://dx.doi.org/10.1002/adma.201870041.
- Chang, K., Ji, W.-F., Li, C.-W., Chang, C.-H., Peng, Y.-Y., Yeh, J.-M., Liu, W.-R., 2014. The effect of varying carboxylic group content in reduced graphene oxides on the anticorrosive properties of PMMA/Graphene composites. EXPRESS Polym. Lett. 8 (December), 908–919. http://dx.doi.org/10.3144/expresspolymlett.2014.92.
- Chauhan, D.S., Quraishi, M.A., Ansari, K.R., Saleh, T.A., 2020. Graphene and graphene oxide as new class of materials for corrosion control and protection: Present status and future scenario. Prog. Org. Coat. 147, 105741. http://dx.doi.org/10.1016/j.porgcoat.2020.105741.
- Cote, L.J., Franklin, K., Jiaxing, H., 2009. Langmuir–Blodgett assembly of graphite oxide single layers. J. Am. Chem. Soc. 131 (3), 1043–1049. http://dx.doi.org/10.1021/ ia806262m.
- Dedkov, Y.S., Fonin, M., 2010. Electronic and magnetic properties of the graphene-ferromagnet interface. New J. Phys. 12 (12), 125004. http://dx.doi.org/10.1088/1367-2630/12/12/125004.
- Dumée, L.F., He, L., Wang, Z., Sheath, P., Xiong, J., Feng, C., Tan, M.Y., et al., 2015. Growth of nano-textured graphene coatings across highly porous stainless steel supports towards corrosion resistant coatings. Carbon 87, 395–408. http: //dx.doi.org/10.1016/j.carbon.2015.02.042.
- Ettefagh, H., Guo, S., 2018. Electrochemical behavior of AISI316l stainless steel parts produced by laser-based powder bed fusion process and the effect of post annealing process. Addit. Manuf. 22, 153–156. http://dx.doi.org/10.1016/j.addma.2018.05.
- Ferrari, A.C., Basko, D.M., 2013. Raman spectroscopy as a versatile tool for studying the properties of graphene. Nature Nanotechnol. 8 (4), 235–246. http://dx.doi.org/ 10.1038/nnano.2013.46.
- He, A., Huang, S., Yun, J.-H., Jiang, Z., Stokes, J., Jiao, S., Wang, L., Huang, H., 2017. The PH-dependent structural and tribological behaviour of aqueous graphene oxide suspensions. Tribol. Int. 116, 460–469. http://dx.doi.org/10.1016/j.triboint.2017. 08.008.
- Hummers, W., Offeman, R., 2022. Preparation of graphitic oxide. J. Am. Chem. Soc. Accessed June 30, 2022. https://pubs.acs.org/doi/pdf/10.1021/ja01539a017.

- Jia, G., Plentz, J., Dellith, J., Dellith, A., Wahyuono, R.A., Andrä, G., 2019. Large area graphene deposition on hydrophobic surfaces, flexible textiles, glass fibers and 3D structures. Coatings 9 (3), 183. http://dx.doi.org/10.3390/coatings9030183.
- Jia, G., Plentz, J., Presselt, M., Dellith, J., Dellith, A., Patze, S., Tölle, F.J., et al., 2017. A double self-assembly process for versatile reduced-graphene-oxide layer deposition and conformal coating on 3D structures. Adv. Mater. Interfaces 4 (23), 1700758. http://dx.doi.org/10.1002/admi.201700758.
- Johnson, D., Dobson, B., Coleman, K., 2015. A manufacturing perspective on graphene dispersions. Curr. Opin. Colloid Interface Sci. 20 (5–6), 367–382. http://dx.doi.org/ 10.1016/j.cocis.2015.11.004.
- Kang, J., Shin, D., Bae, S., Hong, B.H., 2012. Graphene transfer: Key for applications. Nanoscale 4 (18), 5527–5537. http://dx.doi.org/10.1039/C2NR31317K.
- Khan, U., O'Neill, A., Porwal, H., May, P., Nawaz, K., Coleman, J.N., 2012. Size selection of dispersed, exfoliated graphene flakes by controlled centrifugation. Carbon 50 (2), 470-475. http://dx.doi.org/10.1016/j.carbon.2011.09.001.
- Kim, D.J., Quang-Trung, T., Kim, J.I., Suh, Y., Moon, J., Lee, S., Hong, B.H., Woo, Y.S., 2021. Ultrahigh-strength multi-layer graphene-coated Ni film with interface-induced hardening. Carbon 178, 497–505. http://dx.doi.org/10.1016/j.carbon.2021.03.021.
- Kumar, S.S.A., Bashir, S., Ramesh, K., Ramesh, S., 2021. New perspectives on graphene/graphene oxide based polymer nanocomposites for corrosion applications: The relevance of the graphene/polymer barrier coatings. Prog. Org. Coat. 154, 106215. http://dx.doi.org/10.1016/j.porgcoat.2021.106215.
- Kuziel, A.W., Milowska, K.Z., Chau, P.-L., Boncel, S., Koziol, K.K., Yahya, N., Payne, M.C., 2020. The true amphipathic nature of graphene flakes: A versatile 2D stabilizer. Adv. Mater. 32 (34), 2000608. http://dx.doi.org/10.1002/adma. 202000608.
- Munz, M., Giusca, C.E., Myers-Ward, R.L., Kurt Gaskill, D., Kazakova, O., 2015. Thickness-dependent hydrophobicity of epitaxial graphene. ACS Nano 9 (8), 8401–8411. http://dx.doi.org/10.1021/acsnano.5b03220.
- Nayak, S.R., Mohana, K.N.S., 2018. Corrosion protection performance of functionalized graphene oxide nanocomposite coating on mild steel. Surf. Interfaces 11 (June), 63–73. http://dx.doi.org/10.1016/j.surfin.2018.03.002.
- Oliver, W.C., Pharr, G.M., 1992. An improved technique for determining hardness and elastic modulus using load and displacement sensing indentation experiments. J. Mater. Res. 7 (6), 1564–1583. http://dx.doi.org/10.1557/JMR.1992.1564.
- Parhizkar, N., Shahrabi, T., Ramezanzadeh, B., 2017. A new approach for enhancement of the corrosion protection properties and interfacial adhesion bonds between the epoxy coating and steel substrate through surface treatment by covalently modified amino functionalized graphene oxide film. Corros. Sci. 123, 55–75. http://dx.doi.org/10.1016/j.corsci.2017.04.011.
- Park, J., Park, J., 2014. Electrophoretic deposition of graphene oxide on mild carbon steel for anti-corrosion application. Surf. Coat. Technol. 254 (September), 167–174. http://dx.doi.org/10.1016/j.surfcoat.2014.06.007.
- Pharr, G.M., Oliver, W.C., Brotzen, F.R., 1992. On the generality of the relationship among contact stiffness, contact area, and elastic modulus during indentation. J. Mater. Res. 7 (3), 613–617. http://dx.doi.org/10.1557/JMR.1992.0613.
- Pourhashem, S., Vaezi, M.R., Rashidi, A., Bagherzadeh, M.R., 2017. Exploring corrosion protection properties of solvent based epoxy-graphene oxide nanocomposite coatings on mild steel. Corros. Sci. 115 (February), 78–92. http://dx.doi.org/10.1016/ j.corsci.2016.11.008.

- Prasai, D., Tuberquia, J.C., Harl, R., Jennings, G., Bolotin, K., 2022. Graphene: Corrosion-inhibiting coating. ACS Nano Accessed May 31, 2022. https://pubs.acs.org/doi/full/10.1021/nn203507y?casa_token=go3PQb3LU6IAaAAA%3Amd94CSqDCff08OfMQ-CCQLZnS_SD0A26ksYKRiuwTUOimirJKPOrJ145tPeadLC6UlvvUUvA34Z8G-31Fg.
- Qi, K., Yimin, S., Hongwei, D., Xingpeng, G., 2015. A corrosion-protective coating based on a solution-processable polymer-grafted graphene oxide nanocomposite. Corros. Sci. 98, 500–506. http://dx.doi.org/10.1016/j.corsci.2015.05.056.
- Qian, W., Hao, R., Hou, Y., et al., 2009. Solvothermal-assisted exfoliation process to produce graphene with high yield and high quality. Nano Res. 2, 706–712. http://dx.doi.org/10.1007/s12274-009-9074-z.
- Qian, W., Hao, R., Zhou, J., Eastman, M., Manhat, B.A., Sun, Q., Goforth, A.M., Jiao, J., 2013. Exfoliated graphene-supported pt and pt-based alloys as electrocatalysts for direct methanol fuel cells. Carbon 52, 595–604. http://dx.doi.org/10.1016/j. carbon.2012.10.031.
- Schindelholz, E.J., Melia, M.A., Rodelas, J.M., 2021. Corrosion of additively manufactured stainless steels—Process, structure, performance: A review. Corrosion 77 (5), 484–503. http://dx.doi.org/10.5006/3741.
- Shih, C.-J., Lin, S., Sharma, R., Strano, M., Blankschtein, D., 2022. Understanding the PH-dependent behavior of graphene oxide aqueous solutions: A comparative experimental and molecular dynamics simulation study. Langmuir Accessed June 28, 2022. https://pubs.acs.org/doi/full/10.1021/la203607w.
- Stöberl, U., Wurstbauer, U., Wegscheider, W., Weiss, D., Eroms, J., 2022. Morphology and flexibility of graphene and few-layer graphene on various substrates. Appl. Phys. Lett. 93 (5), Accessed July 5, 2022. https://aip.scitation.org/doi/full/10. 1063/1.2968310.
- Su, Y., Kravets, V.G., Wong, S.L., Waters, J., Geim, A.K., Nair, R.R., 2014. Impermeable barrier films and protective coatings based on reduced graphene oxide. Nature Commun. 5 (1), 4843. http://dx.doi.org/10.1038/ncomms5843.
- Tofail, S.A.M., Koumoulos, E.P., Bandyopadhyay, A., Bose, S., O'Donoghue, L., Charitidis, C., 2018. Additive manufacturing: Scientific and technological challenges, market uptake and opportunities. Mater. Today 21 (1), 22–37. http://dx.doi.org/10.1016/j.mattod.2017.07.001.
- Tyagi, P., Goulet, T., Riso, C., Stephenson, R., Chuenprateep, N., Schlitzer, J., Benton, C., Garcia-Moreno, F., 2019. Reducing the roughness of internal surface of an additive manufacturing produced 316 steel component by chempolishing and electropolishing. Addit. Manuf. 25, 32–38. http://dx.doi.org/10.1016/j.addma. 2018.11.001.
- Xiaohui, Y., Lin, Z., Zhang, H., Zhu, H., Liu, Z., Zhong, M., 2015. Protecting carbon steel from corrosion by laser in situ grown graphene films. Carbon 94, 326–334. http://dx.doi.org/10.1016/j.carbon.2015.06.080.
- Xu, H., Zang, J., Yuan, Y., Tian, P., Wang, Y., 2019. In situ preparation of graphene coating bonded to stainless steel substrate via CrC bonding for excellent anticorrosion and wear resistant. Appl. Surf. Sci. 492, 199–208. http://dx.doi.org/10.1016/ j.apsusc.2019.06.197.
- Zhang, W.-B., Chen, C., Tang, P.-Y., 2014. First-principles study for stability and binding mechanism of graphene/Ni(111) interface: Role of VdW interaction. J. Chem. Phys. 141 (4), 044708. http://dx.doi.org/10.1063/1.4890728.